Enhancing the thermoelectric performance of cold sintered calcium cobaltite ceramics through optimised heat-treatment

Jincheng Yu [a], Mikko Nelo [b], Xiaodong Liu [a], Shouqi Shao [a], Bing Wang [a], Sarah J. Haigh [a], Heli Jantunen [b], Robert Freer [a,*]

[a] *Department of Materials, University of Manchester, Manchester M13 9PL, United Kingdom*
[b] *Microelectronics Research Unit, University of Oulu, P. O. Box 4500, FI-90014, Finland*

ABSTRACT

Cold sintering is a promising technology for preparing electronic materials, enabling densification at low temperature, but rarely employed for thermoelectrics. Herein, high-quality $Ca_{2.7}Bi_{0.3}Co_{3.92}O_{9+\delta}$ ceramics were synthesised by a combination of cold sintering and annealing processes. Stoichiometric mixtures of raw materials were calcined once or twice at 1203 K for 12 h in air, and then cold sintered at 673 K for 60 min under a pressure of 85 MPa, followed by annealing at 1203 K for 12 h or 24 h in air. The effects of the calcination processes and annealing conditions on the thermoelectric performance of cold sintered samples were investigated. By optimising heat-treatment, the formation of secondary phases, texture development and porosity were controlled, leading to enhanced electrical conductivity and reduced thermal conductivity. Consequently, at 800 K there was 85% increase in power factor and 35% increase in ZT (value of 0.15) compared to previous studies.

1. Introduction

Thermoelectric (TE) materials, which enable the conversion between waste heat and electricity, provide opportunities to alleviate the energy crisis. The conversion efficiency of a TE material is characterised by the figure of merit $ZT = \sigma S^2 T/\kappa$, where σ is the electrical conductivity, S is the Seebeck coefficient, T is the absolute temperature and κ is the thermal conductivity [1]. The most commonly adopted strategy for improving the conversion efficiency is either maximising the power factor (σS^2) or minimising the thermal conductivity (κ). Calcium cobaltite ($Ca_3Co_4O_9$) is a promising TE oxide because of its intrinsically low thermal conductivity arising from the misfit layered structure [2]. However, it is difficult to prepare dense calcium cobaltite ceramics by pressure-less sintering, due to the complex, layered structure as well as the mismatch between the decomposition temperature (about 1209 K in air for $Ca_3Co_{3.93}O_{9+\delta}$, determined by DSC) [3] and the eutectic temperature (about 1623 K in air, deduced from the Ca–Co–O phase diagram) [3].

Cold sintering, an emerging sintering technique, is able to densify ceramic bodies at low temperatures (< 700 K) and at low cost with simple processing, through dissolution-based transport mechanisms and substantial capillarity effects [4,5]. To date, inorganic materials densified by cold sintering have been employed in the fields of ferroelectrics [6], piezoelectrics [7], microwave dielectrics [8], fuel cell cathodes [9], and refractories [10] . However, only a few attempts have been made to fabricate cold sintered cobaltite ceramics. Funahashi et al. [11] prepared ZnO-$Ca_3Co_4O_9$ multilayer ceramics by cold sintering but mainly focused on the output voltage of the thermoelectric module, while the ZT value of the material was not evaluated. Santos et al. [12] investigated the effects of fabrication routes (solid state reaction and cold sintering) on the thermoelectric performance of calcium cobaltite, but the TE performance of the cold sintered samples was heavily restricted by the low densification ($< 80\%$ theoretical).

In this work, highly dense ($> 90\%$ theoretical) calcium cobaltite ceramics were prepared by cold sintering, using the optimal chemical composition ($Ca_{2.7}Bi_{0.3}Co_{3.92}O_{9+\delta}$) reported in earlier studies [13,14]. The influence of calcination processes for powders and annealing conditions for cold sintered ceramics on the thermoelectric response was studied in detail. By optimising the heat-treatment process, the formation of poorly conducting secondary phases was suppressed, and there was significant development in texture. In comparison with previous investigations of calcium cobaltite prepared by cold sintering there was 85% enhancement in power factor and 35% increase in ZT values [11, 12] as a result of the modified microstructure.

Table 1

Heat-treatment conditions and sample codes.

Calcination conditions	Annealing conditions	Sample Code	Sample
1203 K for 12 h (once)	–	S1P	Powder
	1203 K for 0 h	S1A0	Ceramic
	1203 K for 12 h	S1A12	Ceramic
	1203 K for 24 h	S1A24	Ceramic
1203 K for 12 h (twice)	–	S2P	Powder
	1203 K for 0 h	S2A0	Ceramic
	1203 K for 12 h	S2A12	Ceramic
	1203 K for 24 h	S2A24	Ceramic

2. Materials and methods

Raw materials of $CaCO_3$ (Sigma-Aldrich, 99.8%), Bi_2O_3 (Sigma-Aldrich, 99.9%) and Co_3O_4 (Alfa Aesar, 99.7%) were mixed according to the ratios required for the optimal composition: $Ca_{2.7}Bi_{0.3}Co_{3.92}O_{9+\delta}$. After wet-milling and drying, the powders were divided into two batches and calcined in air at 1203 K for 12 h, either once or twice. Subsequently, in the cold sintering step, performed as in our earlier work (with molybdate and ferrite materials) [15], 3.6 g of single-fired or double fired powder was mixed individually with 0.40 g of 1 M acetic acid. The mixtures were transferred into a 20 mm diameter steel die for compaction; 100 μm thick stainless steel plates were used to protect the sample from the pistons. The die was then pressed under 390 MPa for 60 min at room temperature, after which the pressure was gradually lowered to 85 MPa. When the pressure was stable, the press plates were heated to 673 K for 60 min, followed by cooling to 373 K before releasing the pressure. All samples were removed from the die at room temperature and subsequently annealed at 1203 K for either 12 or 24 h in air. With one set of as-fired samples (zero time anneal) we have three samples for each set of calcine conditions (Table 1).

The bulk density (ρ) and porosity were determined by the Archimedes' method. X-ray diffraction patterns (XRD) were collected from the solid sample surface perpendicular to the pressing direction by a PANaytical X'Pert Pro diffractometer (Cu Kα). Lotgering factors (reflecting the degree of grain orientation) for the annealed cold sintered calcium cobaltite ceramics were determined via Eq. 1 [16], based on the collected XRD data and details from the standard PDF card (JCPDS: # 05–001–0461) [17]:

$$LF = (p - p_0) / (1 - p_0) \tag{1}$$

where LF is the Lotgering factor, $p = \Sigma I \,(00\,l) / \Sigma I \,(hkl)$ (ΣI is the total X-ray counts associated with the indexed peaks for the obtained samples) and $p_0 = \Sigma I_0 \,(00\,l) / \Sigma I_0 \,(hkl)$ (ΣI_0 is the total X-ray counts associated with the peaks for randomly oriented samples calculated from the standard PDF card).

The microstructure and chemical compositions were examined using a Tescan MIRA3 field emission gun – scanning electron microscope (FEG-SEM) equipped with an energy dispersive X-ray spectroscopy (EDX) detector. In order to estimate the volume fractions of different phases in the cold sintered samples, phase quantification was performed through phase contrast [18] based on backscattered electron (BSE) SEM images, using different threshold intensities [19] identified using Image J software. The crystal structure was characterised by transmission electron microscopy (TEM) using a FEI Tecnai G2 20 and a Talos F200X (both operated at 200 kV). Scanning transmission electron microscopy (STEM) and STEM-EDX were performed using a Talos F200X equipped with a Super-X 4 silicon drift detector EDX system (collection solid angle 0.9 srad). X-ray photoelectron spectroscopy (XPS) was undertaken using a Kratos Axis Ultra Hybrid XPS (Al Kα). The XPS data were fitted by the CASA XPS software via a mix of Lorentzian and Gaussian characters. Electrical conductivity and Seebeck coefficient measurements were carried out using an ULVAC ZEM-3 in low-pressure He. The specific heat capacity (C_p) was measured by a Netzsch STA-449 C in N_2. The thermal diffusivity (α) was determined by a Netzch LFA-427 in Ar. The thermal conductivity (κ) was calculated from: $\kappa = \rho \alpha C_p$. Both the electronic transport and thermal properties were measured perpendicular to the pressing direction.

3. Results and discussion

3.1. Physical properties

All the as-sintered samples were dark grey in colour and crack-free. Before annealing, highly dense, cold sintered $Ca_{2.7}Bi_{0.3}Co_{3.92}O_{9+\delta}$ ceramics, exhibit densities of ~ 90% theoretical (S1A0: 4.42 g/cm^3, S2A0: 4.29 g/cm^3; Fig. S1 in Supporting Information (SI)). As the annealing time increased, the bulk density decreased slightly, whilst the porosity increased; the highest porosity was 13.1% for S2A24 (Fig. S1b).

3.2. XRD analysis

Fig. 1 shows XRD patterns for calcined $Ca_{2.7}Bi_{0.3}Co_{3.92}O_{9+\delta}$ powders and cold sintered $Ca_{2.7}Bi_{0.3}Co_{3.92}O_{9+\delta}$ ceramics annealed in different ways. The main phase in all patterns is indexed as monoclinic $Ca_3Co_{3.744}O_{9.176}$ (JCPDS: # 05-001-0461). Traces of three minor phases including $Bi_2Ca_3Co_2O_9$ (JCPDS: # 52-0125), $Ca_3Co_2O_6$ (JCPDS: # 51-
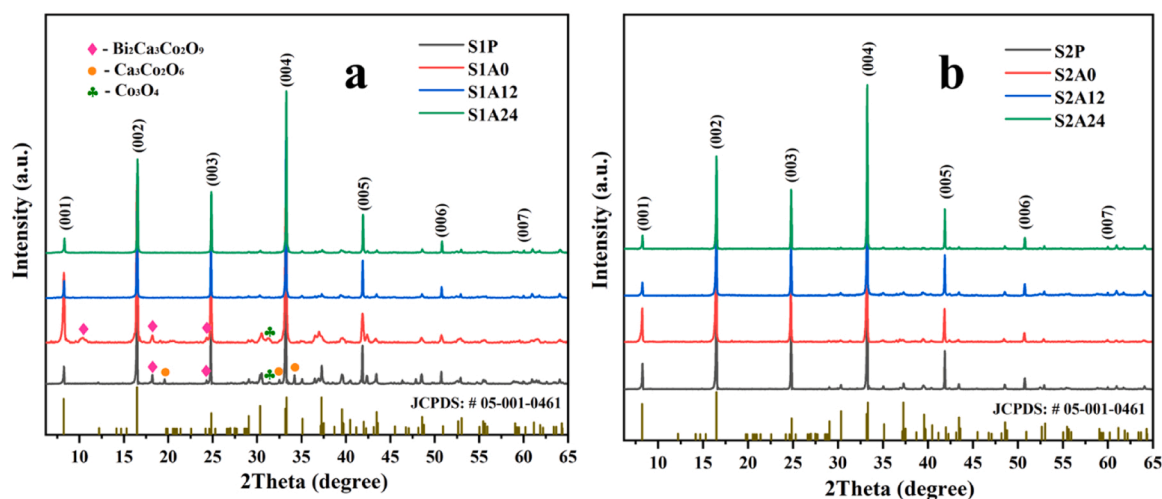
Fig. 1. XRD patterns for calcined $Ca_{2.7}Bi_{0.3}Co_{3.92}O_{9+\delta}$ powders and cold sintered $Ca_{2.7}Bi_{0.3}Co_{3.92}O_{9+\delta}$ ceramics annealed in different ways (a: samples prepared from single-calcined powders; b: samples prepared from double-calcined powders).

Table 2

Calculated Lotgering factors for cold sintered $Ca_{2.7}Bi_{0.3}Co_{3.92}O_{9+\delta}$ ceramics.

Sample ID	p	p_0	Lotgering factor
S1A0	0.778	0.305	0.68
S1A12	0.812	0.305	0.73
S1A24	0.832	0.305	0.76
S2A0	0.800	0.305	0.71
S2A12	0.858	0.305	0.79
S2A24	0.881	0.305	0.83

0311) and Co_3O_4 (JCPDS: # 42-0461) were detected in the single-fired powders (Fig. 1a) with the fraction of secondary phases being significantly reduced at longer annealing times. By contrast, X-ray pure calcium cobaltite powders were synthesised by the double calcination process (Fig. 1b). Furthermore, the increased intensity for peaks belonging to the {00 l} family in the annealed samples suggest preferred grain growth along the *c* axis.

The calculated Lotgering factors (LF) derived from the data in Fig. 1 are shown in Table 2. It is evident that the LF values increase with increasing annealing time and the number of calcination processes, indicating that the strongest texture was developed in the S2A24 sample. Optimising the heat-treatment can also help to eliminate secondary phases that hinder primary grain connectivity [14].

3.3. SEM-EDS analysis

Fig. S2 presents backscattered electron (BSE) SEM images of calcined $Ca_{2.7}Bi_{0.3}Co_{3.92}O_{9+\delta}$ powders before milling. The single-fired powders (S1P in Fig. S2a) exhibit more aggregation than the double-fired powders (S2P in Fig. S2b). Compared to the S1P sample, the S2P sample shows an obvious reduction in the amount of bright secondary phases, suggesting that double calcination promotes the complete reaction to form calcium cobaltite. BSE SEM images for the polished surfaces of $Ca_{2.7}Bi_{0.3}Co_{3.92}O_{9+\delta}$ ceramics are presented in Fig. 2. The chemical composition and distribution of phases in the cold sintered ceramics processed under different heat-treatment conditions were determined by EDS and SEM image analysis (Table S1 and S2; Fig. S2 and S3 in **SI**). In addition to the plate-like grey grains of the primary calcium cobaltite phase in S1A0, there are three minor phases (Fig. 2a): the irregular bright grains (Bi-rich compared to the primary phase); irregular dark grains ($Ca_2Co_2O_5$) and granular grey grains (Co_3O_4). By annealing at 1203 K the secondary phases were efficiently reduced (Figs. 2b and 2c) with the $Ca_2Co_2O_5$ (dark phase) being almost eliminated (Fig. S4a in SI). Compared to S1A0, the twice calcined S2A0 contains a smaller volume fraction of minor phases (Fig. 2d). Interestingly, in S2A0, the newly formed Ca-Co-O compound (dark phase) shows calcium deficiency compared to $Ca_2Co_2O_5$, and the chemical composition of the granular grey phase approaches CoO, indicating that the phase composition can be modified by optimising heat-treatment. Although there is a similar reduction of secondary phases with increasing annealing time for S2A12 and S2A24 (Figs. 2e and 2f; Fig. S4b in SI), there is an obvious increase in grain size and porosity with the increase in annealing time up to 24 h (Fig. 2f). The increase in porosity is probably due to volatilisation of Bi-rich phases [20] and enhanced liquid-solid mass transfer [21] during the prolonged annealing.

Fig. 3 shows secondary electron SEM images of fracture surfaces for cold sintered $Ca_{2.7}Bi_{0.3}Co_{3.92}O_{9+\delta}$ ceramics. Compared to as-sintered calcium cobaltite ceramics (S1A0 and S2A0) where the grain
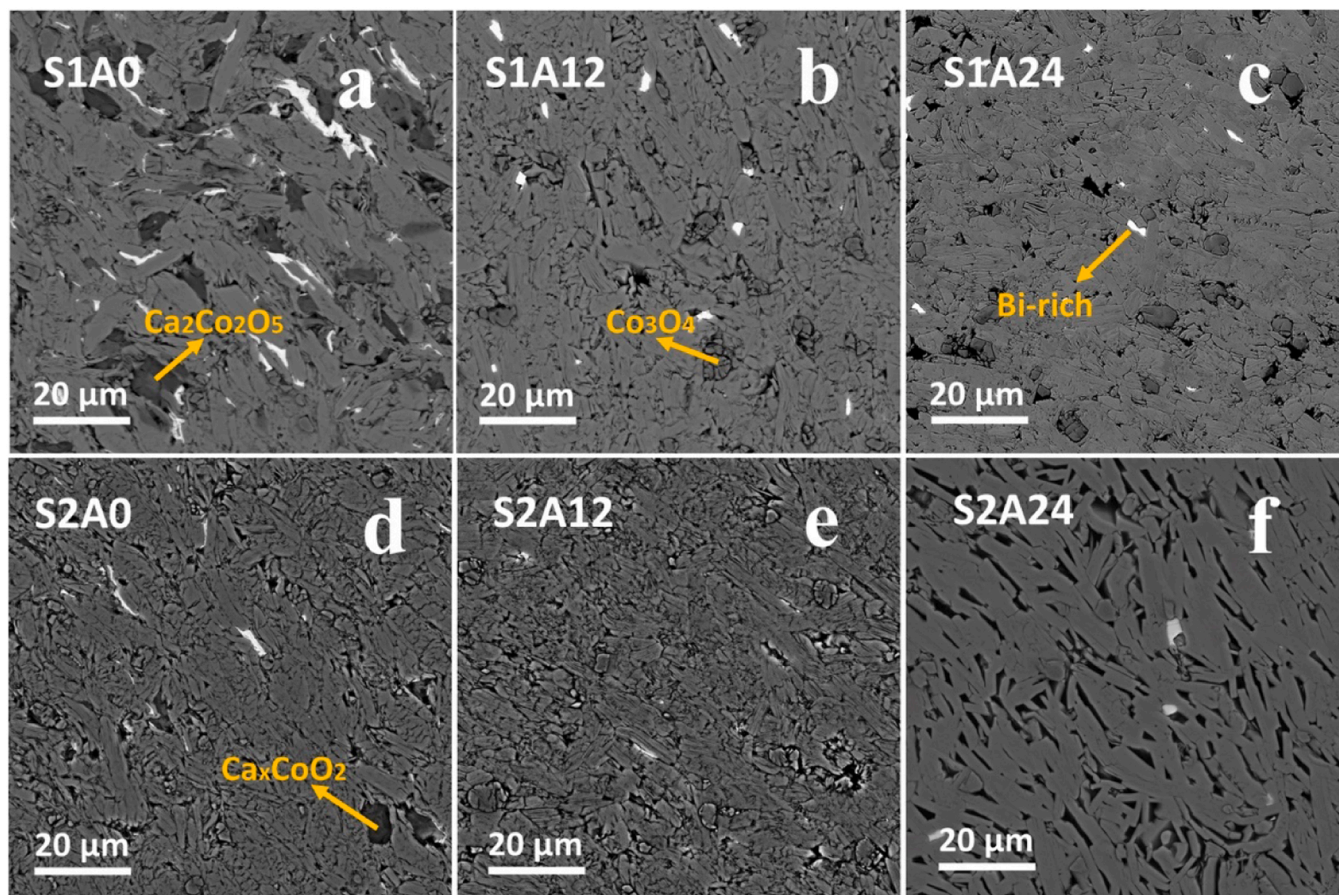
Fig. 2. Backscattered electron SEM images for polished surfaces of cold sintered $Ca_{2.7}Bi_{0.3}Co_{3.92}O_{9+\delta}$ ceramics processed under different cold sintering and annealing heat-treatment conditions (sample codes are given in Table 1).
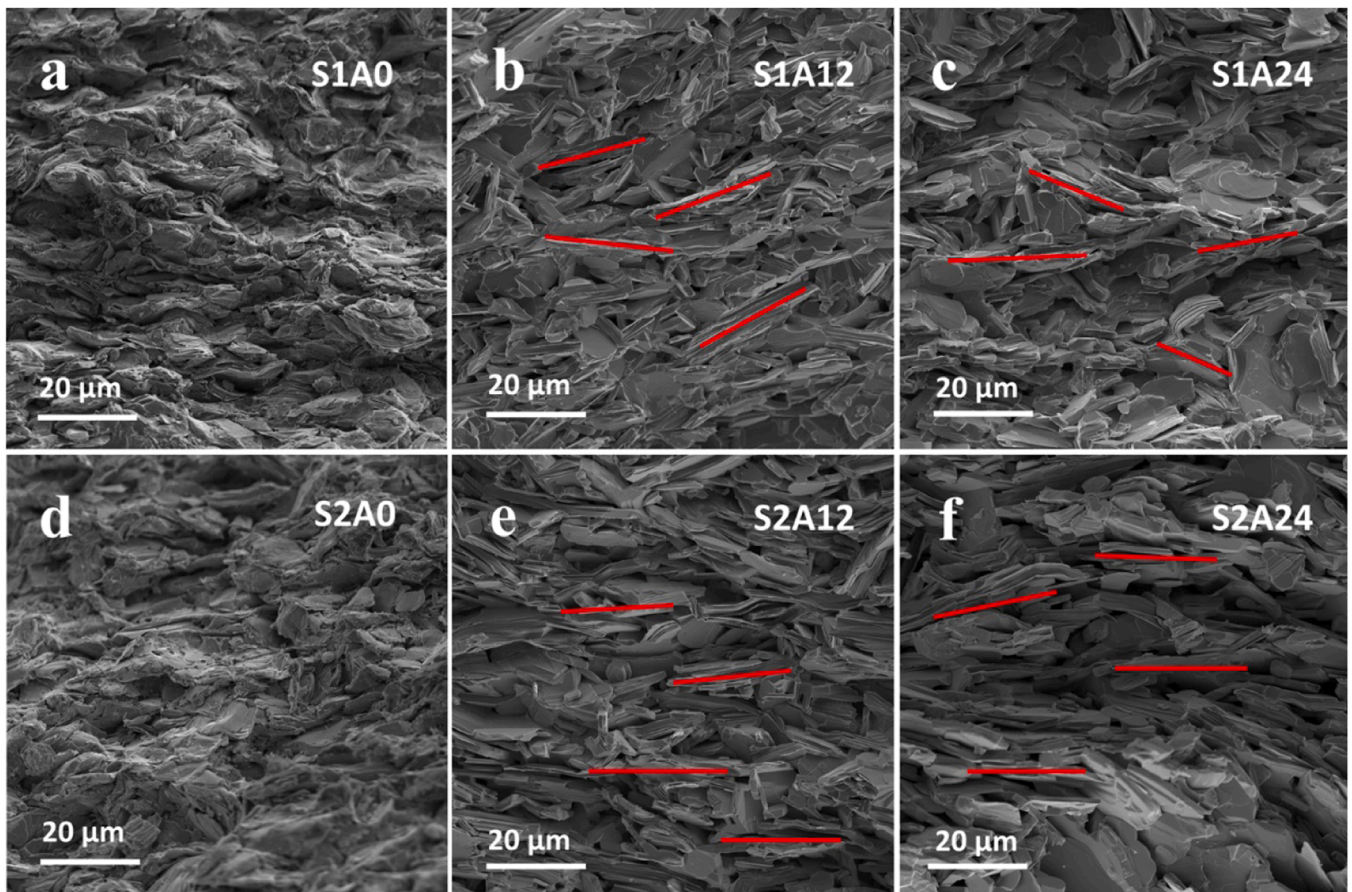
Fig. 3. Secondary electron SEM images of fracture surfaces for cold sintered $Ca_{2.7}Bi_{0.3}Co_{3.92}O_{9+\delta}$ ceramics (the grain alignment in the annealed samples is highlighted by the red lines).
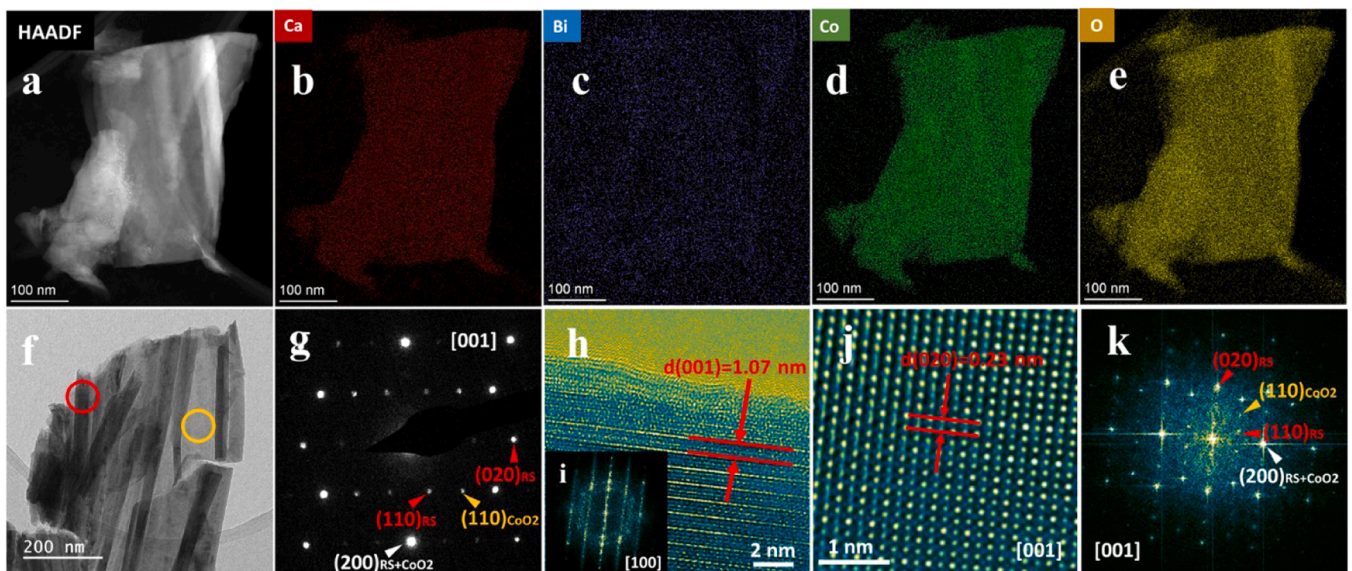

Fig. 4. STEM and TEM data for S2A24 sample: (a) High angle annular dark field (HAADF) STEM image; (b-e) STEM-EDS elemental maps for the region shown in (a); (f) low magnification TEM image; (g) SAED pattern from the yellow circular region in (f); (h) HRTEM image of the red circular region in (f); (i) FFT image for the region shown in (h); (j) Fourier filtered HRTEM image of the yellow circular region in (f); (k) FFT image corresponding to (j).

arrangement is more disordered, there was clear development of texture with increasing annealing time and doubling of the calcination process; the plate-like grains are better aligned in the S2A24 sample, consistent with the trend in Lotgering factors (Table 2).

3.4. TEM and STEM analysis

In order to verify the crystal structure, STEM and TEM data were collected from S2A24 as a representative sample (Fig. 4). In the STEM-
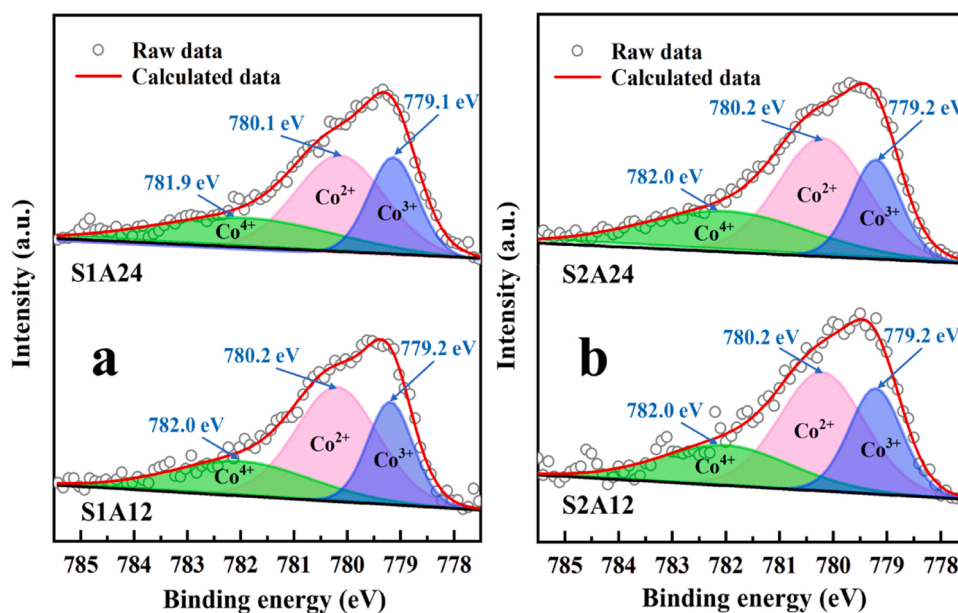
Fig. 5. High-resolution XPS Co2p 3/2 spectra for annealed cold sintered $Ca_{2.7}Bi_{0.3}Co_{3.92}O_{9+\delta}$ ceramics.

EDS elemental maps, the uniform elemental distribution of Ca, Co and O with slight contrast for Bi, confirms the successful doping of bismuth in the calcium cobaltite grains (Fig. 4a–e). The typical plate-like features are highlighted in a grain with dark and bright contrast in Fig. 4f, and the [001] oriented selected area electron diffraction (SAED) pattern (from the yellow circular region in Fig. 4f) confirms a misfit layered structure (Fig. 4g). The two sets of diffraction spots belong to the rock salt layer (red arrows) and CoO_2 layer (yellow arrow); they share a common *a* lattice parameter but have different *b* lattice parameters. The noise-filtered high resolution transmission electron microscopy (HRTEM) image for this region of the sample demonstrates the atomic arrangements of the crystal when viewed along the [001] zone axis, where a d-spacing of 0.23 nm corresponds to the (020) crystal plane (Fig. 4j); its corresponding fast Fourier transform (FFT) image shows the same pattern as the SAED in Fig. 4g. The HRTEM and FFT image of the crystal viewed along the [100] zone-axis (Figs. 4h and i) yields an (001) d-spacing of 1.07 nm, consistent with that expected for the (001) crystal plane of calcium cobaltite. These results match well with TEM data reported by Seo et al. [22] and Yubuta et al. [23] and confirm the crystal structure determined by XRD.

3.5. XPS analysis

As there are considerable amounts of Co-containing secondary phases in the unannealed cold sintered samples, the contributions from different phases to the concentrations of different cobalt ions are complex and difficult to distinguish unambiguously. XPS characterisation was therefore performed on the annealed cold sintered samples; the volume fractions of the primary calcium cobaltite phase reach about 90% and it is believed to dominate the generation of hole carriers for the material. Fig. 5 presents high-resolution XPS Co2p 3/2 spectra for annealed cold sintered $Ca_{2.7}Bi_{0.3}Co_{3.92}O_{9+\delta}$ ceramics. Three peaks from different cobalt ions are revealed in the spectra; the peaks at 781.9–782.0 eV (green colour) are assigned to Co^{4+}, the peaks at 780.1–780.2 eV (pink colour) are ascribed to Co^{2+} and the peaks at 779.1–779.2 eV (blue colour) are attributed to Co^{3+}. These results are consistent with the Co XPS data in earlier studies and confirm the presence of three kinds of cobalt ions in the crystal lattice of calcium cobaltite [24–26].

The concentrations of the different cobalt ions in the annealed samples, determined from the XPS data in Fig. 5, are summarised in

Table 3
Concentrations of cobalt ions in annealed cold sintered $Ca_{2.7}Bi_{0.3}Co_{3.92}O_{9+\delta}$ ceramics determined by XPS.

Sample Code	Co^{3+} (%)	Co^{2+} (%)	Co^{4+} (%)	$Co^{4+}/(Co^{3+}+Co^{4+})$ (%)
S1A12	24.5	49.9	25.6	51.1
S1A24	25.0	44.8	30.2	54.7
S2A12	25.9	46.3	27.8	51.8
S2A24	23.6	49.9	26.5	52.9

Table 3. For all the annealed cold sintered samples, the ratio of $[Co^{4+}/(Co^{3+}+Co^{4+})]$ varies only slightly, from 51% to 55%, averaging 52.6%. As the presence of Co^{4+} among Co^{3+} ions is believed to regulate the concentration of holes in calcium cobaltite [27], this data does not suggest any significant variation in carrier concentration.

3.6. Electrical transport

Fig. 6 shows the electrical transport properties of cold sintered $Ca_{2.7}Bi_{0.3}Co_{3.92}O_{9+\delta}$ ceramics as a function of temperature. The electrical conductivity (σ) for all samples increases with increasing temperature (Fig. 6a), indicating semiconducting behaviour; the σ varies from 5.2 to 99.9 S/cm at 323 K and from 88.6 to 120.1 S/cm at 800 K. The positive Seebeck coefficients (S) in Fig. 6b confirm a hole conduction mechanism; the coefficients vary from 133.5 to 159.0 μV/K at 323 K, and from 150.1 to 183.0 μV/K at 800 K. Compared to the cold sintered calcium cobaltite ceramics reported in earlier studies [11,12] (exhibiting σ of 60–70 S/cm at 800 K; Seebeck coefficients of 120–150 μV/K at 800 K) the electrical conductivity (σ) in this work (120.1 S/cm at 800 K) represents at least 70% enhancement while the corresponding Seebeck coefficients (150.1 μV/K at 800 K) are similar.

For the samples prepared from the single-fired powders, the lowest σ is recorded for S1A0, whilst σ values for S1A12 and S1A24 are nearly triple that for S1A0. This can be ascribed to the increased fractions of the primary phase (calcium cobaltite) and the reduction of poorly conducting phases (Fig. S4). Only slight changes in S are observed between S1A12 and S1A24, whereas the values are significantly lower than for S1A0. On the basis of the first term in Eq. 2 (Drude model) [28]:

$$S = C_e/n + \pi^2 k^2 T/3e([\partial \ln\mu(\varepsilon)/\partial\varepsilon]_{\varepsilon = Ef}) \tag{2}$$

where C_e is the electronic specific heat capacity, n is the carrier
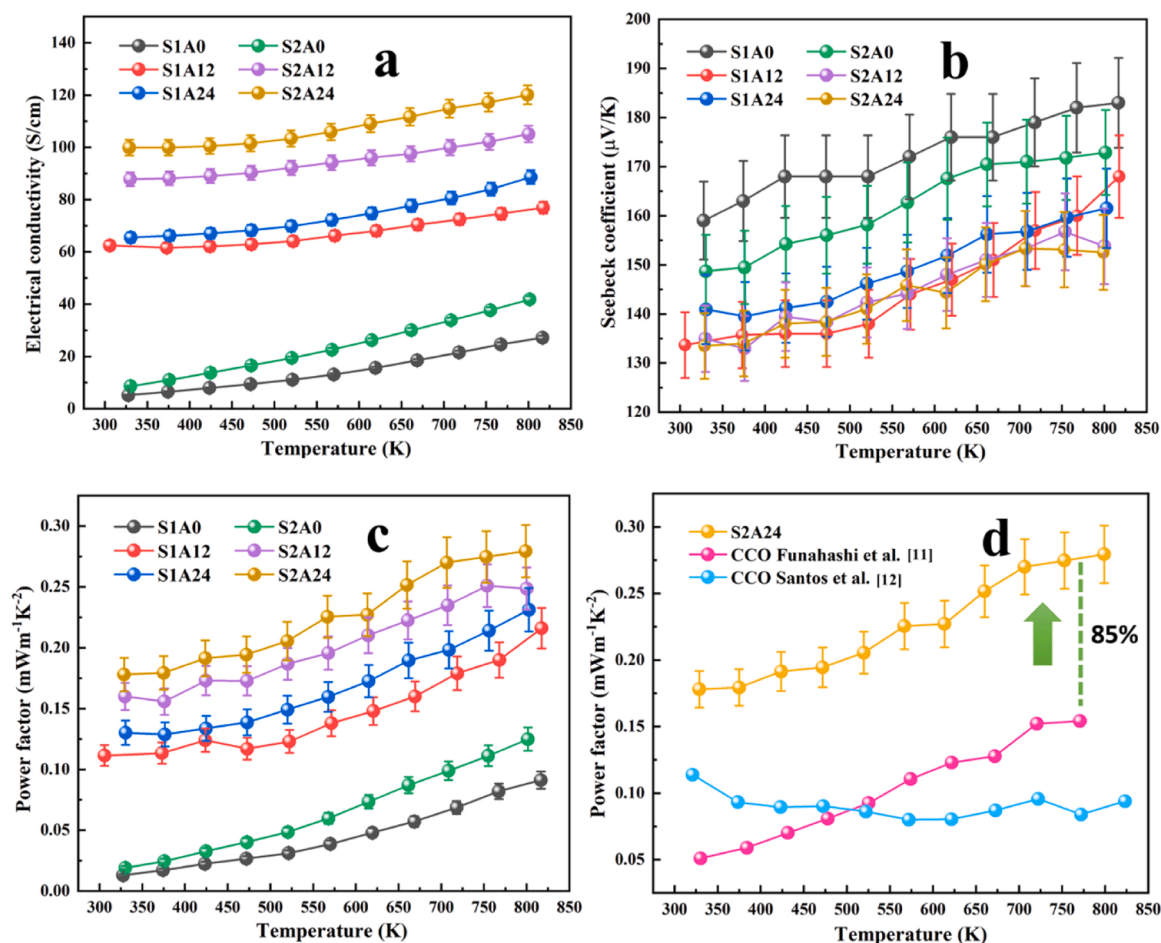
Fig. 6. Electrical conductivity (a), Seebeck coefficient (b) and power factor (c) for cold sintered $Ca_{2.7}Bi_{0.3}Co_{3.92}O_{9+\delta}$ ceramics as a function of temperature, and (d) power factor compared with previous work [11,12].

concentration, k is the Boltzmann constant, T is absolute temperature, $\mu(\varepsilon)$ is the energy correlated carrier mobility and E_f is the Fermi level, it is inferred (from the Seebeck coefficients) that the carrier concentration (n) is similar for S1A12 and S1A24, and much higher than that for S1A0. Similar variations in σ and S are found for the samples prepared from double-fired powders (Fig. 6a and b).

Before annealing, sample S1A0 exhibited lower σ than S2A0, mainly due to the lower fraction of the primary phase (Fig. S4). The corresponding Seebeck coefficients (S) for S1A0 are larger than those for S2A0, fitting well with the Drude model. After annealing at 1203 K for 12 h, sample S2A12 also exhibits enhanced σ compared to S1A12. As there is negligible variation in the value of $[Co^{4+}/(Co^{3+}+Co^{4+})]$ for S1A12 and S2A12 (Table 3), n should be similar for both. This is also supported by the similar Seebeck coefficients (S) for S1A12 and S2A12 (Fig. 6b). Therefore, the increased σ should result from enhanced carrier mobility (μ) according to Eq. 3:

$$\sigma = ne\mu \quad (3)$$

where n is the carrier concentration, e is the electronic charge and μ is the carrier mobility. It was reported that texture development and larger grain size lead to decreased in-plane grain boundary density, thereby lowering energy barriers at grain boundaries and hence a larger μ [29, 30]. Here, both the Lotgering factors (Table 2) and SEM images of fracture surfaces (Fig. 3) show that greater texture is achieved in S2A12 compared to S1A12, thereby encouraging enhanced mobility. Similarly, S2A24 exhibits higher σ than S1A24 when the annealing time is extended to 24 h.

Fig. 6c shows that the highest power factor of 0.28 $mWm^{-1}K^{-2}$ was

obtained for S2A24 at 800 K; this value represents at least 85% enhancement compared to the power factors reported in earlier investigations for cold sintered calcium cobaltite ceramics (0.08–0.15 $mWm^{-1}K^{-2}$ at 800 K) [11,12] (Fig. 6d).

In order to provide insight into the relationship between the electronic transport properties and the correlative factors, the values for σ and S at 800 K are plotted as a function of annealing time, Lotgering factor and porosity (Fig. 7). It is noted that σ increases for all the samples (Fig. 7a), whilst the corresponding S values decrease with increasing annealing time (Fig. 7b). In addition, S2 samples show significantly higher σ but slightly lower S values than S1 samples. These results indicate that the power factor can be enhanced by the double calcination process and prolonging the annealing time. It was found that the change in σ is positively correlated with Lotgering factor (Fig. 7c), whereas the Seebeck coefficients show a negative correlation (Fig. 7d). Stronger texture can lead to reduced in-plane grain boundary density and hence decreased energy barrier at grain boundaries, thereby increasing the carrier mobility and lowering the thermopower [31,32]. Interestingly, the σ and S values show an opposite trend with increasing porosity, increasing and decreasing respectively (Figs. 7e and 7f). Generally, poorer densification is associated with an increase in the energy barrier at grain boundaries, thereby leading to reduced carrier mobility and higher thermopower. This contradictory behaviour is ascribed to the dominating effects of texture development compared to that of porosity.

3.7. Thermal transport

The samples prepared from double-fired powders (S2P) were
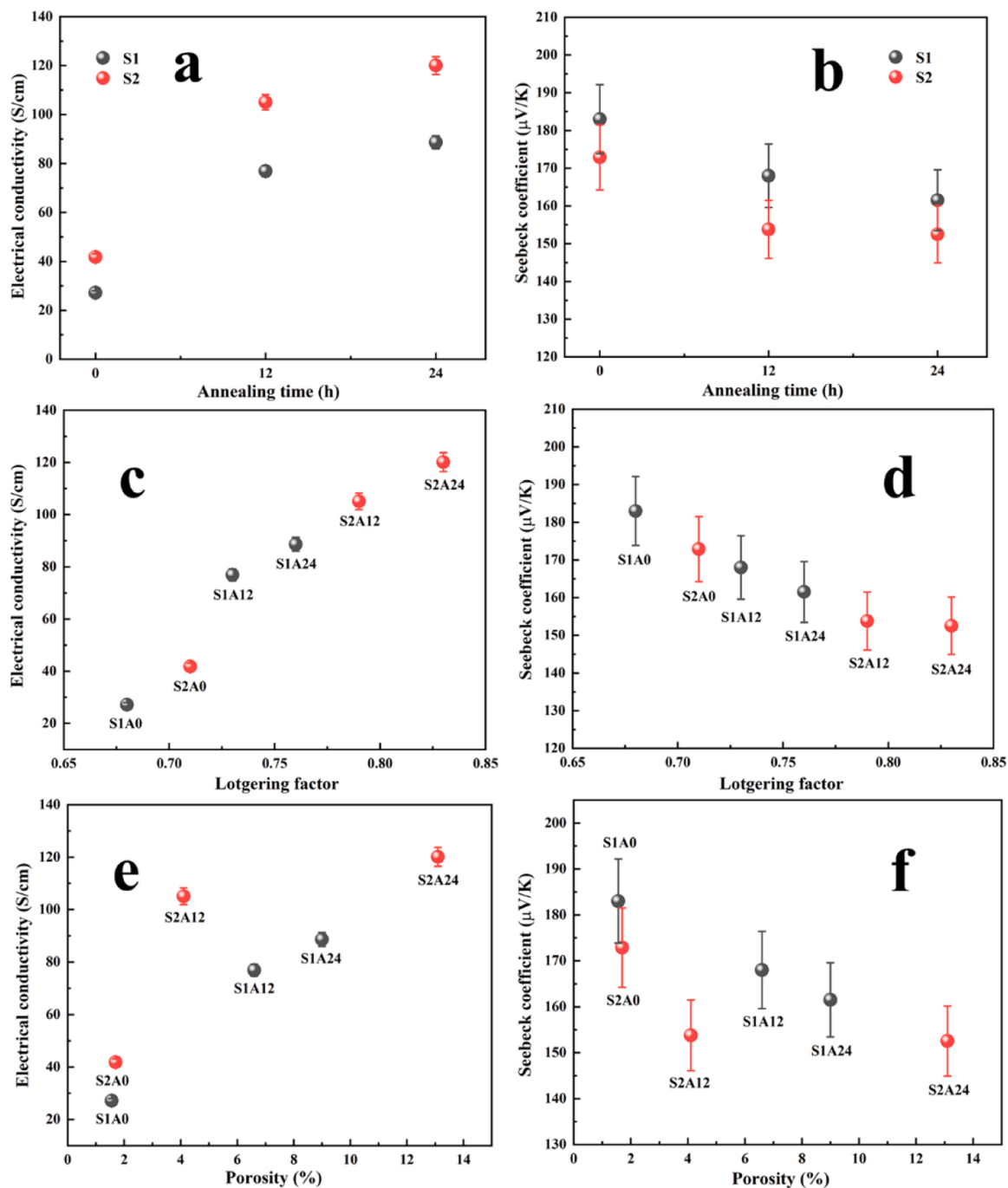
Fig. 7. Electrical conductivity and Seebeck coefficients at 800 K for cold sintered $Ca_{2.7}Bi_{0.3}Co_{3.92}O_{9+\delta}$ ceramics as a function of annealing time (a, b), Lotgering factor (c, d) and porosity (e, f).

selected for detailed thermal conductivity analysis, because they showed significantly enhanced electrical transport behaviour. The total thermal conductivity and the corresponding electronic and lattice components for cold sintered $Ca_{2.7}Bi_{0.3}Co_{3.92}O_{9+\delta}$ ceramics are presented in Fig. 8. It can be seen that there is an increase in total thermal conductivity (κ), after a 12 h anneal (S2A12), compared to the as-fired ceramics S2A0 (Fig. 8a), but a significant reduction to 1.5 $Wm^{-1}K^{-1}$ at 800 K when the annealing time is extended to 24 h (S2A24). Fig. 8b presents the electronic ($\kappa_{electronic}$) and lattice ($\kappa_{lattice}$) thermal conductivities determined from the Wiedemann-Franz law, using Eqs. 4 and 5 [33]:

$$\kappa_{electronic} = L\sigma T \tag{4}$$

$$\kappa = \kappa_{electronic} + \kappa_{lattice} \tag{5}$$

where L is the Lorenz constant (2.45×10^{-8} $W\Omega K^{-2}$ for free electrons) and T is absolute temperature. The phonon contribution at 323 K represents ~ 95% of the total, but decreases to ~ 85% of the total at 800 K. Sample S2A12 exhibits similar $\kappa_{lattice}$ but a higher $\kappa_{electronic}$ compared to S2A0; the slight enhancement in κ is attributed to the higher σ (longer annealing time). By contrast, the significant reduction in κ for S2A24 results mainly from the lower $\kappa_{lattice}$, which indicates enhanced phonon scattering. It is acknowledged that point defect scattering is dominated by the solute atoms, through variations in atomic mass and size (described by the Debye–Callaway model using Equations S1-S4 in SI) [34,35]. As bismuth solubility in S2A12 and S2A24 is very similar (Bi/(Bi+Ca) ≈ 0.1; Table S2), the point defect scattering is expected to
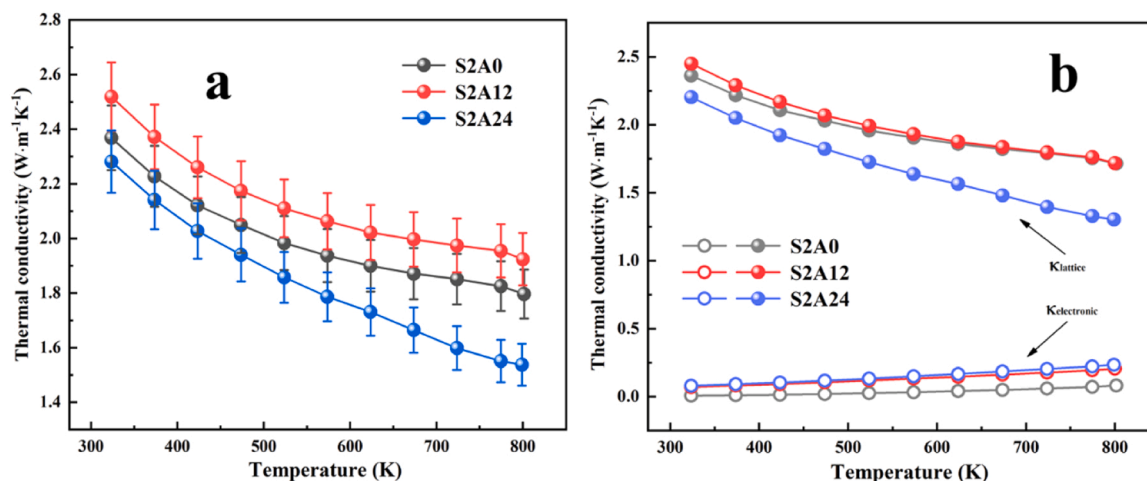
Fig. 8. Temperature dependence of: (a) total thermal conductivity and (b) electronic and lattice thermal conductivity for cold sintered $Ca_{2.7}Bi_{0.3}Co_{3.92}O_{9+\delta}$ ceramics.
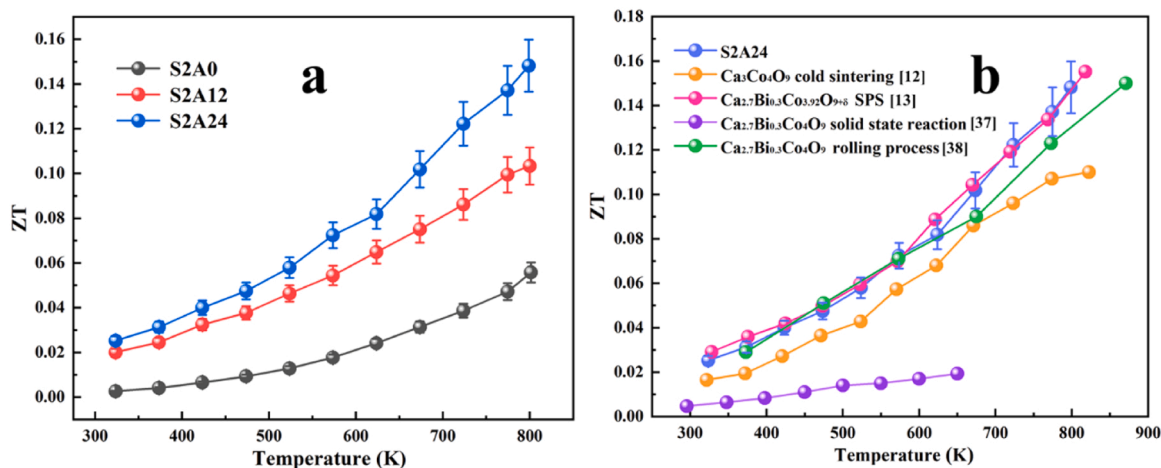

Fig. 9. (a) Temperature dependence of ZT values for cold sintered $Ca_{2.7}Bi_{0.3}Co_{3.92}O_{9+\delta}$ ceramics and (b) comparison of ZT values with calcium cobaltite prepared by different fabrication routes in earlier studies [12,13,37,38].

be similar in these two materials. Although stronger texture development, by increasing annealing time from 12 h to 24 h (Table 2), can lead to weaker in-plane grain boundary scattering, there is also a significant increase in porosity from 4% to 13% (Fig. S1b). The pores can also act as scattering centres to enhance phonon scattering, and their effects on total thermal conductivity can be evaluated using Eq. 6 [36]:

$$\kappa = \kappa_0(1 - \nu)/(1 + \beta\nu) \tag{6}$$

where κ_0 is the thermal conductivity of an ideal material with zero porosity, ν is the volume fractions of pores and β is the pore shape factor ($\beta = 1.0–3.0$ for spherical pores). Therefore, S2A24 exhibits lower $\kappa_{lattice}$ than S2A12 mainly because of the higher fraction of pores (Fig. 2f).

3.8. Thermoelectric figure of merit

Fig. 9a shows the temperature dependence of ZT values for cold sintered $Ca_{2.7}Bi_{0.3}Co_{3.92}O_{9+\delta}$ ceramics. The maximum ZT of 0.15 is achieved in S2A24 at 800 K, because of the enhanced power factor and reduced thermal conductivity (Figs. 6c and 8a). In comparison to previous work on cold sintered calcium cobaltite [12], the S2A24 data presented here for ZT value (0.15 at 800 K) represents 35% enhancement. Indeed, this ZT value is superior to that for the solid state synthesised sample [37] and is also comparable to data reported for spark plasma sintered (SPS)-processed and rolling-processed samples [13,38],

demonstrating the considerable potential for cold sintering technology in fabricating thermoelectric devices.

4. Conclusions

This investigation demonstrates a simple approach to enhancing the thermoelectric performance of $Ca_{2.7}Bi_{0.3}Co_{3.92}O_{9+\delta}$ ceramics by cold sintering in combination with heat-treatment. Through double calcination of powders at 1203 K for 12 h and post-sinter annealing of ceramics at 1203 K for 24 h, the presence of secondary phases was efficiently reduced, thereby enhancing the texture, and increasing the volume fraction of the main phase (calcium cobaltite). The electrical conductivity was enhanced by the increased concentration and mobility of carriers. The Lotgering factors, reflecting the degree of grain orientation, are positively correlated with the electrical conductivity but negatively correlated with the Seebeck coefficients, due to the reduction of in-plane grain boundary density and energy barriers. In addition, the pores generated during annealing can act as scattering centres, enhancing phonon scattering, thereby reducing thermal conductivity. As a result, a maximum power factor of 0.28 $mWm^{-1}K^{-2}$ and ZT value of 0.15 were achieved at 800 K for the double sintered sample with the longest (24 h) annealing time (S2A24). These values represents enhancements of approximately 85% and 35% respectively, compared to published data for cold sintered calcium cobaltite.

Declaration of Competing Interest

The authors declare that they have no known competing financial interests or personal relationships that could have appeared to influence the work reported in this paper.

Acknowledgements

Appendix A. Supporting information

Supplementary data associated with this article can be found in the online version at doi:10.1016/j.jeurceramsoc.2022.03.017.

References

[1] L.-D. Zhao, J. He, D. Berardan, Y. Lin, J.-F. Li, C.-W. Nan, N. Dragoe, BiCuSeO oxyselenides: new promising thermoelectric materials, Energy Environ. Sci. 7 (2014) 2900–2924.

[2] C.-H. Lim, W.-S. Seo, S. Lee, Y.S. Lim, J.-Y. Kim, H.-H. Park, S.-M. Choi, K.H. Lee, K. Park, Anisotropy of the thermoelectric figure of merit (ZT) in textured $Ca_3Co_4O_9$ ceramics prepared by using a spark plasma sintering process, J. Korean Phys. Soc. 66 (2015) 794–799.

[3] D. Sedmidubský, V. Jakeš, O. Jankovský, J. Leitner, Z. Sofer, J. Hejtmánek, Phase equilibria in Ca–Co–O system, J. Solid State Chem. 194 (2012) 199–205.

[4] J. Guo, R. Floyd, S. Lowum, J.-P. Maria, T. Herisson de Beauvoir, J.-H. Seo, C. A. Randall, Cold sintering: progress, challenges, and future opportunities, Annu. Rev. Mater. Res. 49 (2019) 275–295.

[5] J. Guo, S.S. Berbano, H. Guo, A.L. Baker, M.T. Lanagan, C.A. Randall, Cold sintering process of composites: bridging the processing temperature gap of ceramic and polymer materials, Adv. Funct. Mater. 26 (2016) 7115–7121.

[6] H. Guo, A. Baker, J. Guo, C.A. Randall, Protocol for ultralow-temperature ceramic sintering: an integration of nanotechnology and the cold sintering process, ACS Nano 10 (2016) 10606–10614.

[7] D. Wang, H. Guo, C.S. Morandi, C.A. Randall, S. Trolier-McKinstry, Cold sintering and electrical characterization of lead zirconate titanate piezoelectric ceramics, APL Mater. 6 (2018) 16101.

[8] D. Wang, D. Zhou, S. Zhang, Y. Vardaxoglou, W.G. Whittow, D. Cadman, I. M. Reaney, Cold-sintered temperature stable $Na_{0.5}Bi_{0.5}MoO_4$–Li_2MoO_4 microwave composite ceramics, ACS Sustain. Chem. Eng. 6 (2018) 2438–2444.

[9] J.-H. Seo, J. Guo, H. Guo, K. Verlinde, D.S.B. Heidary, R. Rajagopalan, C. A. Randall, Cold sintering of a Li-ion cathode: $LiFePO_4$-composite with high volumetric capacity, Ceram. Int. 43 (2017) 15370–15374.

[10] H. Guo, T.J.M. Bayer, J. Guo, A. Baker, C.A. Randall, Current progress and perspectives of applying cold sintering process to ZrO_2-based ceramics, Scr. Mater. 136 (2017) 141–148.

[11] S. Funahashi, H. Guo, J. Guo, A.L. Baker, K. Wang, K. Shiratsuyu, C.A. Randall, Cold sintering and co-firing of a multilayer device with thermoelectric materials, J. Am. Ceram. Soc. 100 (2017) 3488–3496.

[12] A.M. dos Santos, D. Thomazini, M.V. Gelfuso, Cold sintering and thermoelectric properties of $Ca_3Co_4O_9$ ceramics, Ceram. Int. 46 (2020) 14064–14070.

[13] J. Yu, K. Chen, F. Azough, D.T. Alvarez-Ruiz, M.J. Reece, R. Freer, Enhancing the thermoelectric performance of calcium cobaltite ceramics by tuning composition and processing, ACS Appl. Mater. Interfaces 12 (2020) 47634–47646.

[14] J. Yu, Y. Chang, E. Jakubczyk, B. Wang, F. Azough, R. Dorey, R. Freer, Modulation of electrical transport in calcium cobaltite ceramics and thick films through microstructure control and doping, J. Eur. Ceram. Soc. 41 (2021) 4859–4869.

[15] M. Väätäjä, H. Kähäri, J. Juuti, H. Jantunen, Li_2MoO_4-based composite ceramics fabricated from temperature- and atmosphere-sensitive MnZn ferrite at room temperature, J. Am. Ceram. Soc. 100 (2017) 3626–3635.

[16] J.L. Jones, E.B. Slamovich, K.J. Bowman, Critical evaluation of the Lotgering degree of orientation texture indicator, J. Mater. Res. 19 (2004) 3414–3422.

[17] R. Shimonishi, M. Hagiwara, S. Fujihara, Fabrication of highly textured $Ca_3Co_4O_9$ ceramics with controlled density and high thermoelectric power factors, J. Eur. Ceram. Soc. 40 (2020) 1338–1343.

[18] A. Sotelo, S. Rasekh, E. Guilmeau, M.A. Madre, M.A. Torres, S. Marinel, J.C. Diez, Improved thermoelectric properties in directionally grown $Bi_2Sr_2Co_{1.8}O_y$ ceramics by Pb for Bi substitution, Mater. Res. Bull. 46 (2011) 2537–2542.

[19] A. Faes, A. Hessler-Wyser, D. Presvytes, C.G. Vayenas, J. Van Herle, Nickel–zirconia anode degradation and triple phase boundary quantification from microstructural analysis, Fuel Cells 9 (2009) 841–851.

[20] C. Di, J.-H. Pan, S.-T. Dong, Y.-Y. Lv, X.-J. Yan, J. Zhou, S.-H. Yao, H. Lu, V. E. Gusev, Y.-F. Chen, M.-H. Lu, Ultralow cross-plane lattice thermal conductivity caused by Bi–O/Bi–O interfaces in natural superlattice-like single crystals, CrystEngComm 21 (2019) 6261–6268.

[21] Z. Shi, F. Gao, J. Zhu, J. Xu, Y. Zhang, T. Gao, M. Qin, Influence of liquid−phase sintering on microstructure and thermoelectric properties of $Ca_3Co_4O_9$−based ceramics with Bi_2O_3 additive, J. Mater. 5 (2019) 711–720.

[22] W. Seo, S. Lee, Y. Lee, M. Lee, Y. Masuda, K. Koumoto, High-resolution transmission electron microscopy study of $Ca_3Co_4O_9$, Microscopy 53 (2004) 397–401.

[23] K. Yubuta, X. Huang, T. Miyazaki, T. Kajitani, High-resolution electron microscopy study of $[(Ca,Bi)CoO_3]_{0.62}CoO_2$, J. Phys. Soc. Jpn. 77 (2008) 94603.

[24] Y. Huang, B. Zhao, S. Lin, R. Ang, Y. Sun, Enhanced thermoelectric performance induced by Cr doping at Ca-sites in $Ca_3Co_4O_9$ system, J. Am. Ceram. Soc. 97 (2014) 3589–3596.

[25] K. Park, D.A. Hakeem, J.S. Cha, Synthesis and structural properties of thermoelectric $Ca_{3-x}Ag_xCo_4O_{9+\delta}$ powders, Dalton Trans. 45 (2016) 6990–6997.

[26] H. Liu, G.C. Lin, X.D. Ding, J.X. Zhang, Mechanical relaxation in thermoelectric oxide $Ca_{3-x}Sr_xCo_4O_{9+\delta}$ (x= 0, 0.25, 0.5, 1.0) associated with oxygen vacancies, J. Solid State Chem. 200 (2013) 305–309.

[27] D. Moser, L. Karvonen, S. Populoh, M. Trottmann, A. Weidenkaff, Influence of the oxygen content on thermoelectric properties of $Ca_{3-x}Bi_xCo_4O_{9+\delta}$ system, Solid State Sci. 13 (2011) 2160–2164.

[28] Y. Wang, Y. Sui, X. Wang, W. Su, X. Liu, Enhanced high temperature thermoelectric characteristics of transition metals doped $Ca_3Co_4O_{9+\delta}$ by cold high-pressure fabrication, J. Appl. Phys. 107 (2010) 33708.

[29] Y. Zhou, I. Matsubara, W. Shin, N. Izu, N. Murayama, Effect of grain size on electric resistivity and thermopower of $(Ca_{2.6}Bi_{0.4})Co_4O_9$ thin films, J. Appl. Phys. 95 (2003) 625–628.

[30] T. Sun, H.H. Hng, Q.Y. Yan, J. Ma, Enhanced high temperature thermoelectric properties of Bi-doped c-axis oriented $Ca_3Co_4O_9$ thin films by pulsed laser deposition, J. Appl. Phys. 108 (2010) 83709.

[31] Z.Y. Liu, F.P. Zhang, J.X. Zhang, X. Zhang, Q.M. Lu, X.Y. Yang, Enhanced electrical transport by texture modulation and co-doping for $Ca_3Co_4O_{9+\delta}$ materials, Results Phys. 6 (2016) 203–208.

[32] B. Madavali, H.-S. Kim, K.-H. Lee, S.-J. Hong, Enhanced Seebeck coefficient by energy filtering in Bi-Sb-Te based composites with dispersed Y_2O_3 nanoparticles, Intermetallics 82 (2017) 68–75.

[33] R. Franz, G. Wiedemann, Ueber die Wärme-Leitungsfähigkeit der Metalle, Ann. Phys. 165 (1853) 497–531.

[34] G.-K. Ren, J.-L. Lan, K.J. Ventura, X. Tan, Y.-H. Lin, C.-W. Nan, Contribution of point defects and nano-grains to thermal transport behaviours of oxide-based thermoelectrics, NPJ Comput. Mater. 2 (2016) 16023.

[35] Y. Zheng, M. Zou, W. Zhang, D. Yi, J. Lan, C.-W. Nan, Y.-H. Lin, Electrical and thermal transport behaviours of high-entropy perovskite thermoelectric oxides, J. Adv. Ceram. 10 (2021) 377–384.

[36] J.L. Mi, T.J. Zhu, X.B. Zhao, J. Ma, Nanostructuring and thermoelectric properties of bulk skutterudite compound $CoSb_3$, J. Appl. Phys. 101 (2007) 54314.

[37] I.V. Matsukevich, A.I. Klyndyuk, E.A. Tugova, A.N. Kovalenko, A.A. Marova, N. S. Krasutskaya, Thermoelectric properties of $Ca_{3-x}Bi_xCo_4O_{9+\delta}$ (0.0 ⩽ x ⩽ 1.5) ceramics, Inorg. Mater. 52 (2016) 593–599.

[38] J.W. Park, D.H. Kwak, S.H. Yoon, S.C. Choi, Thermoelectric properties of highly oriented $Ca_{2.7}Bi_{0.3}Co_4O_9$ fabricated by rolling process, J. Ceram. Soc. Jpn. 117 (2009) 643–646.